Article

CFD Investigation on Hydrodynamic Resistance of a Novel Subsea Shuttle Tanker

Yihan Xing [ID]**, Marek Jan Janocha, Guang Yin** [ID] **and Muk Chen Ong *** [ID]

Department of Mechanical and Structural Engineering and Materials Science, Faculty of Science and Technology, University of Stavanger, 4036 Stavanger, Norway; yihan.xing@uis.no (Y.X.); marek.j.janocha@uis.no (M.J.J.); guang.yin@uis.no (G.Y.)
* Correspondence: muk.c.ong@uis.no

Abstract: The Subsea Shuttle Tanker (SST) was proposed by Equinor as an alternative to subsea pipelines and surface tankers for the transportation of liquid carbon dioxide (CO_2) from existing offshore/land facilities to marginal subsea fields. In contrast to highly weather-dependent surface tanker operations, the SST can operate in any condition underwater. Low resistance is paramount to achieving maximum range. In this paper, the resistance of the SST at an operating forward speed of 6 knots (3.09 m/s) and subject to an incoming current velocity of 1 m/s is computed using Computational Fluid Dynamics (CFD). The Delayed Detached Eddy Simulation (DDES) method is used. This method combines features of Reynolds-Averaged Navier–Stokes Simulation (RANS) in the attached boundary layer parts at the near-wall regions, and Large Eddy Simulation (LES) at the unsteady, separated regions near to the propeller. The force required to overcome forward resistance is calculated to be 222 kN and agrees well with experimental measurements available in the open literature. The corresponding power consumption is calculated to be 927 kW, highlighting the high efficiency of the SST. The method presented in this paper is general and can be used for resistance optimization studies of any underwater vessel.

Keywords: subsea technology; computational fluid dynamics; resistance calculation

1. Introduction

The Subsea Shuttle System (SST) as illustrated in Figure 1 is a novel subsea transportation system or 'cargo train' proposed by Equinor ASA [1,2]. It is conceived as a possible alternative to subsea pipelines, umbilical, and tanker ships. The proposed design is a large submersible propelled using renewable energy with a length of 100 to 200 m and a diameter of 10 to 20 m. The shuttle is primarily designed to be operated at a fixed water depth below the sea surface. The SST is proposed for the transportation of liquid carbon dioxide (CO_2) from an offshore facility to a subsea well, where the CO_2 can be injected. However, it can be also configured to carry other types of cargo:

- It can carry hydrocarbons from a subsea well to a riser base with risers connected to a floating production unit (FPU) or land-based facility for processing.
- It can make use of pressure vessels mounted onboard to carry chemical fluids typically injected into subsea wells, such as methanol and glycol (MEG).
- It can transport electricity to subsea equipment. This can be achieved by storing the electrical power using onboard battery banks and transferring this to the subsea equipment while docked.
- It can also be configured to carry tools, structures, and modules required for subsea construction and intervention.

Figure 1. Equinor subsea shuttle tanker.

The SST uses an aft propeller as its main propulsion and can have directional thrusters incorporated for vector control. Generally, the SST will travel at slow speeds to limit its exposure to large drag forces and thereby reducing battery consumption. The shuttle operation is not weather dependent because it travels subsea, i.e., it is not exposed to wind and waves. The operation can be conducted even in severe weather conditions without any interaction with surface vessels. It can also utilize the external hydrostatic pressure and temperature in its design through a pressure compensating system, see Xing et al. [3] and Ma et al. [4]. Safety of the marine operations will be also enhanced, as the SST can operate remotely or autonomously outside of conventional working conditions which are normally manned.

SST as a form of maritime automation has several key advantages as discussed by Krestschmann et al. [5]:

- The SST can avoid accidents induced by human factors.
- Submarine accidents are catastrophic since rescue and evacuation can be extremely difficult underwater. The cost of unexpected accidents will be significantly reduced for the SST as it is unmanned.
- The SST's cargo capacity can be maximized as it does not require human support systems such as ventilation systems, freshwater tanks, control rooms, living quarters, or kitchens. This also means lower energy consumptions.

Further, the SST reduces field development costs significantly by eliminating one or more of the subsea pipelines, umbilicals, storage tanks, offshore loading systems, tankers, and marine operations costs. This will also help reduce the overall carbon footprint and the environmental impact of the field development.

The SST has the potential to contribute significantly to the 2030 target of limiting global mean temperature rise to 2 °C by operating as cargo transport between small subsea and existing large offshore fields or land facilities, as illustrated in Figure 2. The CCSA [6] indicated that as much as 90% of CO_2 emitted from fossil fuel-based electrical generation and industrial activity can be captured. According to IEA [7], large-scale CCS adoption can provide a CCS capacity of 10 Gigatons per year by 2050. Due to their lower levels of CO_2 storage capacity, small subsea fields are not generally further investigated, as the installation and maintenance of a permanent riser base and FPU would not be an economically viable solution.
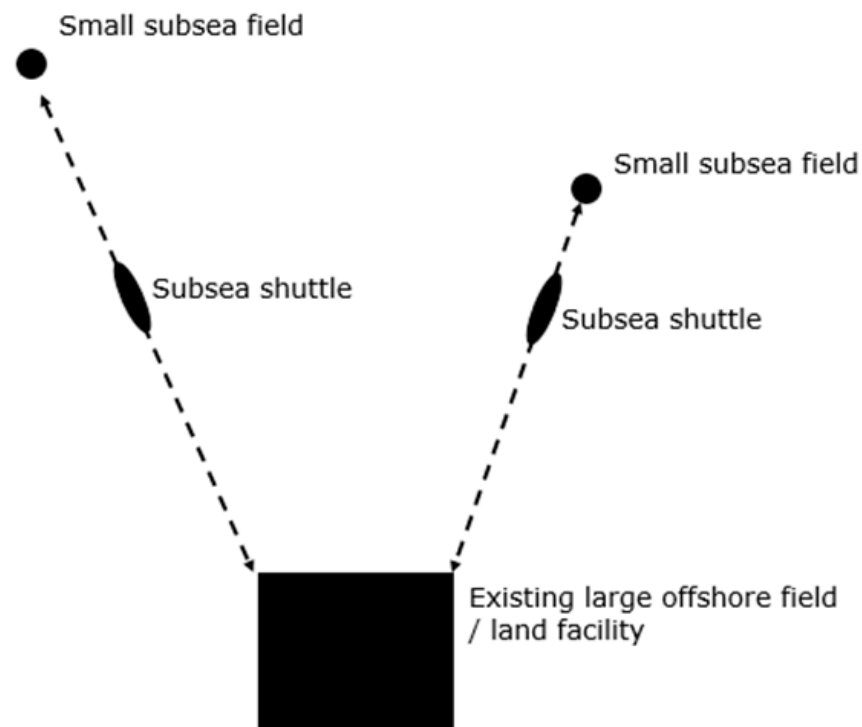
Figure 2. Subsea shuttles deployed to carry cargo between small subsea fields and an existing large offshore field or land facility [3].

Detailed design considerations and baseline design presented by Xing et al. [3] and Ma et al. [4] highlighted the importance of low drag resistance to maximize the SST's working range. This paper will compute the resistance coefficient for the concept hull of a version of Equinor's SST travelling with forward speed. Only the case of flow aligned with the main longitudinal axis of the hull is considered. Advanced hybrid turbulence modelling Delayed Detached Eddy Simulation (DDES) combining Reynolds-Averaged Navier–Stokes (RANS) approach with Large Eddy Simulation (LES) is applied to provide accurate predictions of the pressure and skin friction coefficients as well as to resolve the large-scale turbulent structures in the aft region of the hull. The simulations are performed using an open-source Computational Fluid Dynamics (CFD) toolbox OpenFOAM (Weller et al. [8]) on a multiprocessor computing cluster. OpenFOAM is an established research and engineering tool based on the finite volume method for solving partial differential equations. Examples of numerical studies performed with OpenFOAM related to submarine hydrodynamics can be found in Katsui et al. [9], Shang et al. [10], Jones et al. [11], and Fureby et al. [12], among many others. The hybrid RANS/LES method presented in this paper is used for the first time to predict the resistance of the innovative SST. The method is general and can be used for resistance optimization studies of any underwater vessel such as the subsea freight-glider [13].

2. Main Design Parameters

The hull dimensions used in the present study are shown in Figure 3. The main design parameters of the SST considered are presented in Table 1. In the present study, the Reynolds number is based on the hull length ($Re_L = u_\infty.L/\nu$, where u_∞ is the flow velocity, L is the hull length, and ν is the kinematic viscosity of the fluid) is equal $Re_L = 3.4 \times 10^8$.
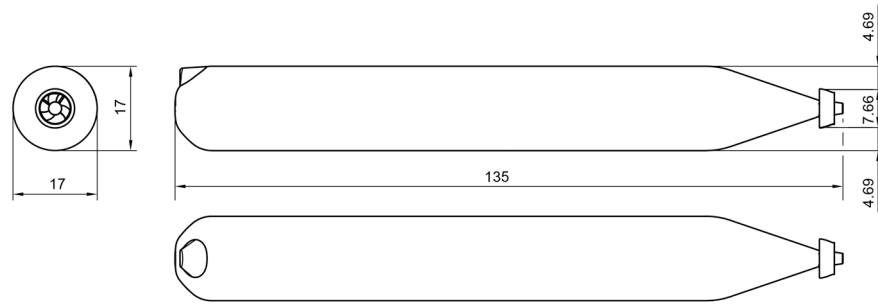
Figure 3. Subsea shuttle tanker's overall dimensions in meters.

Table 1. Main design parameters [14].

Main Design Parameter	Value
Maximum water depth	350 m
Minimum water depth	200 m
Operating speed, U	6 knots (3.09 m/s)
Length, L	135 m
Diameter, D	17 m
Water temperature, T	4 °C
Kinematic viscosity of water at 4 °C, ν	1.626×10^{-6} m^2/s
Maximum current velocity	1 m/s
Reynolds number, Re_L	3.398×10^8

3. Numerical Model

3.1. Numerical Method

Simulations are performed using the open-source CFD toolbox OpenFOAM [15]. OpenFOAM is built based on the finite volume method. In the finite volume method, volume integrals in a partial differential equation that contain a divergence term are converted to surface integrals, using the divergence theorem. These terms are then evaluated as fluxes at the surfaces of each finite volume. In the present study, pressure velocity coupling is solved using the PIMPLE algorithm which combines the Semi-Implicit Method for Pressure Linked Equations (SIMPLE) and Pressure Implicit with Split Operators (PISO) methods. Two outer corrector loops and three inner corrector steps are used. Discretization settings used for terms in the governing equations of the fluid flow are summarized in Table 2.

Table 2. Numerical settings used.

Parameter	Value
Time discretization	Crank–Nicolson, second order
Gradient discretization	Gauss linear, second order
Divergence discretization	Gauss linear, second order
Laplacian discretization	Linear with nonorthogonal correction, second order
Cell-to-face interpolation	Linear, second order
Surface normal gradient discretization	Linear with nonorthogonal correction, second order
Pressure linear solver	Preconditioned Conjugate Gradient
Pressure solver tolerance	10^{-6}
Velocity, k, and ω linear solver	Smooth solver with Gauss–Seidel smoother
Velocity solver tolerance	10^{-8}

3.2. Turbulence Model

Delayed Detached Eddy Simulation (DDES) is a modelling approach that combines features of Reynolds-Averaged Simulation (RANS) in the attached boundary layer parts of the flow and Large Eddy Simulation (LES) in the unsteady, separated flow regions. Flow

around the SST hull is a very high Reynolds number flow with high requirements for the computational mesh resolution within the boundary layers. The RANS method is the most efficient in treating the boundary layer flow due to less stringent mesh requirements as compared to LES. On the other hand, at the aft part of the hull, a highly unsteady flow and formation of turbulent flow structures are of engineering interest for hull design and optimization. The LES method can resolve those structures whereas the RANS method cannot provide the insight of the flow transient behavior due to time averaging. The DDES approach combines both the computational efficiency of the RANS method within the boundary layers and the high fidelity of LES in massively separated flow regions. In the DDES model, an enhanced blending function is implemented to improve the ability of the model to distinguish between LES and RANS regions. The schematic of the DDES approach is depicted in Figure 4.
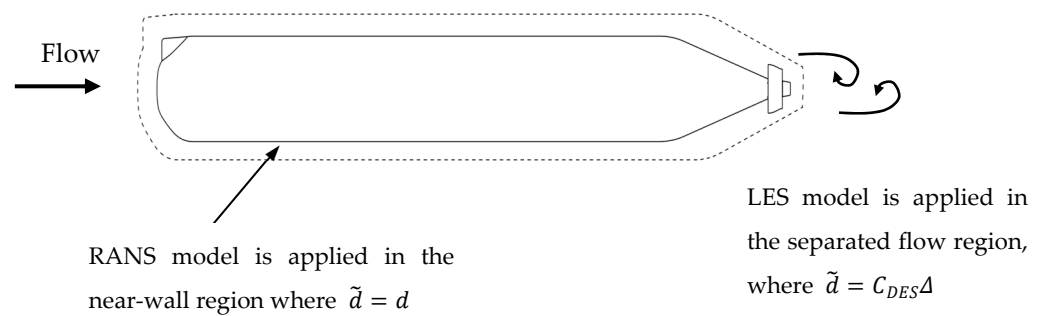

Figure 4. Hybrid RANS/LES approach applied to external flow simulation.

3.3. Computational Domain and Grid

A cylindrical domain with a semi-spherical cap is established around the SST hull as presented in Figure 5. The domain size is given in terms of the hull length, L and the hull cross-sectional diameter, D. These domain settings result in a blockage ratio of 5% which is considered sufficient to avoid the numerical error associated with the numerical influence of the boundary conditions. A schematic of the boundary conditions imposed on the computational domain is shown in Figure 6. A specified incoming flow with $u_x = u_\infty = 3.09 + 1$ m/s and $u_y = u_z = 0$ is used for the velocities and the zero normal gradient is used for the pressure at the inlet. The zero normal gradient is used for the velocity and a reference pressure value is given at the outlet. The sides of the domain are prescribed with zero normal gradient conditions for the velocities and pressure. On the surface of the hull, the no-slip boundary condition is used for the velocities and the zero normal gradient is used for the pressure.
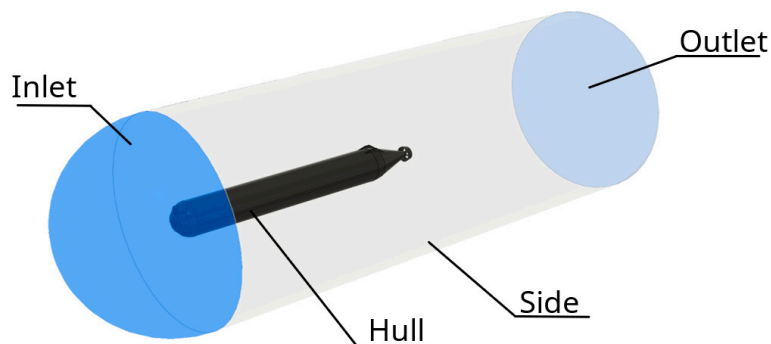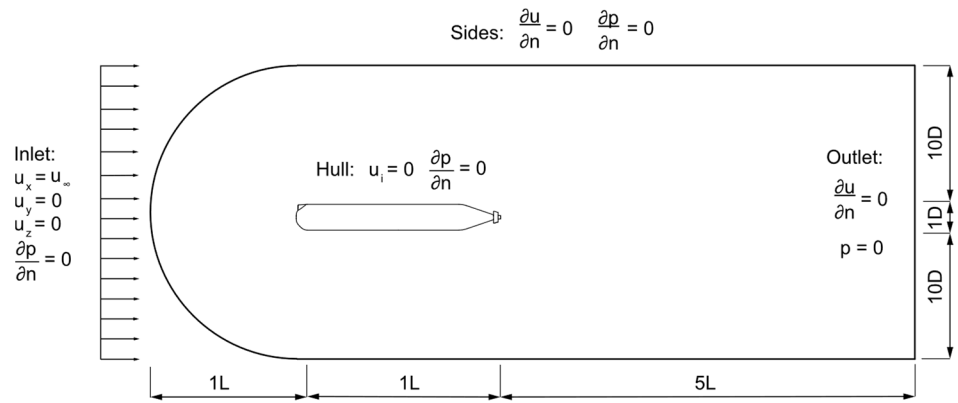

Figure 5. Isometric view of the computational domain with indicated boundary names.

Figure 6. Schematic of the boundary conditions used in the present study.

The surface grids are generated based on the CAD model and presented in Figure 7. The surface mesh is a quad-dominant unstructured mesh designed to well preserve the curvature of the model geometry. The boundary layer mesh is generated by extrusion of the surface mesh to create high-quality prisms. An unstructured tetrahedral mesh is used in the far field. The far-field mesh is refined in the wake area and the vicinity of the hull and the mesh spacing is gradually relaxed further away from the hull. Figure 8 presents an example of the mesh around the front part of the SST and the quality control statistics of the generated grid. The histogram in Figure 8 shows that most cells are high quality (nonorthogonality < 65). The orthogonal cells in the boundary layer mesh are crucial for accurate skin friction prediction.

(**a**)

(**b**)

(**c**)
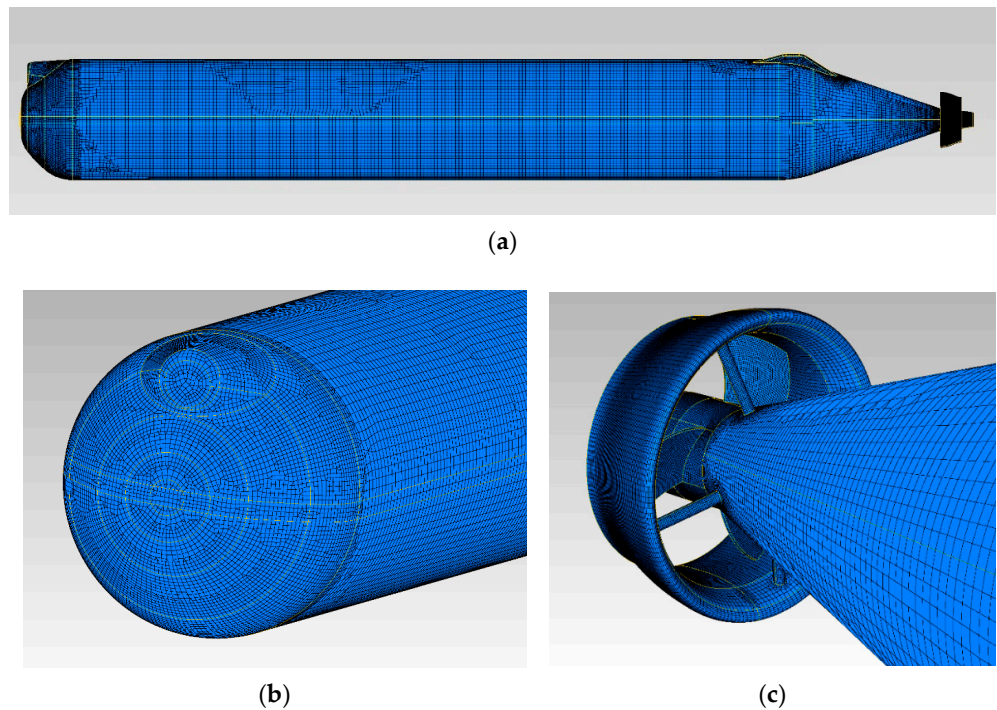
Figure 7. Surface grids generated based on the CAD model of SST hull: (**a**) side view, (**b**) zoom in at the front region, and (**c**) zoom in at the back region.
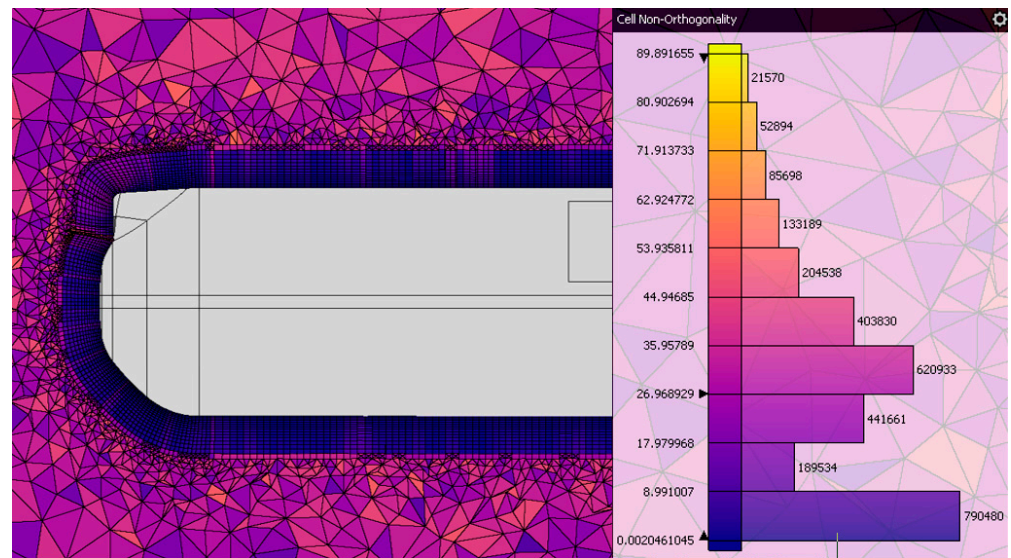
Figure 8. Quality control statistics of the generated volumetric computational grid indicating the dominance of high-quality, orthogonal cells.

3.4. Verification and Validation

The CFD model is verified through the following mesh resolution sensitivity study. This is in accordance with ASME standard V&V 20 [16] for verification and validation of CFD studies. A summary of the grids used in the grid convergence study is given in Table 3. The mesh refinement study is summarized in Table 4. It shows that with the increase of the mesh numbers from 9.8 million to 19.6 million, the relative differences of the total drag force, the pressure drag force, and the viscous drag force between M1 and M2 are all below 5%, which shows that the current model mesh setup of M2 is sufficiently refined for the present analyses.

**Table 3.** Number of cells used in numerical grids used in the grid sensitivity analysis.

Mesh Variant	Number of Cells
M1 Coarse	4.2 million
M2 Medium	9.8 million
M3 Dense	19.6 million

Table 4. Total drag force, pressure, and viscous components of the drag force for computational grids used in the grid sensitivity analysis.

	M1 Coarse	M2 Medium	M3 Dense
Total drag force FD [kN]	244.47	226.08	221.97
Relative error [%]	10.13	1.85	-
Pressure drag component FD, Pressure [kN]	152.07	131.35	126.66
Relative error [%]	20.07	3.7	-
Viscous drag component FD, Viscous [kN]	92.40	94.74	95.31
Relative error [%]	3.06	0.61	-

The CFD model is validated by comparing the present model predictions with the experimental measurements performed on the model submarine hull reported by Jones et al. [17]. The hull geometry and results published by Jones et al. [17] are selected because of their completeness and extensiveness and geometric similarity to the present investigated hull geometry. Figure 9 shows the computational grid and geometry of the model submarine hull (Joubert model) which is the same as used in the experimental study

by Jones et al. [17]. The Joubert model (Figure 9) is a streamlined body of revolution with a length of 1.35 m and a diameter of 0.185 m. The Reynolds number in the present simulation is set to $Re_L = 5.4 \times 10^6$ which is the same as specified in Jones et al. [17].
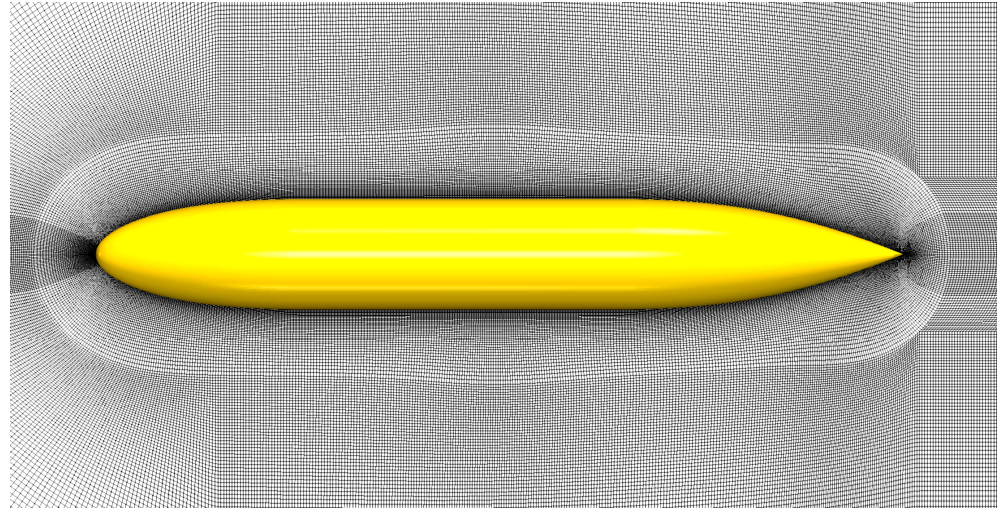

Figure 9. View of computational mesh around Joubert model submarine hull used in the validation study [17].

Comparison of the results of the pressure coefficient (C_p) and the skin friction coefficient (C_f) obtained from the present simulation (using Joubert's hull geometry) with the published experimental values is shown in Figures 10 and 11. The legend in Figures 10 and 11 is as follows:

- Jones et al. (2011) experiment—Experimental results of Joubert's hull geometry from Jones et al. [17]
- Jones et al. (2011) CFD simulation—CFD simulations results of Joubert's hull geometry from Jones et al. [17]
- Present CFD simulation—CFD simulations results of Joubert's hull geometry using the hybrid RANS/LES model which is utilized in this paper's SST hull resistance study
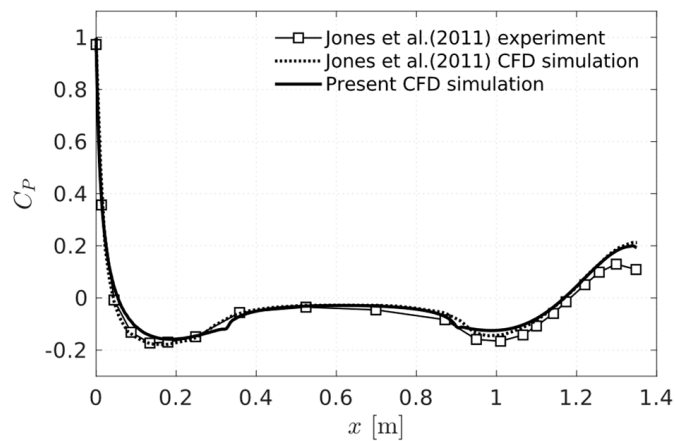
Figure 10. Pressure coefficient along the model submarine hull from present simulation and experimental measurements by Jones et al. [17].
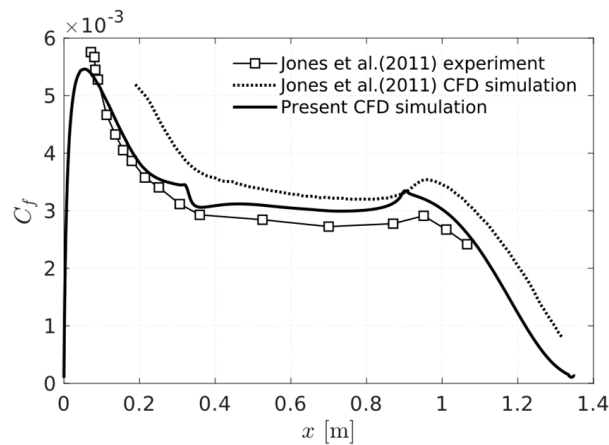
Figure 11. Skin friction coefficient along the model submarine hull from present simulation and experimental measurements by Jones et al. [17].

The value of C_p is calculated as

$$C_p = \frac{p - p_\infty}{\frac{1}{2}\rho U_\infty^2}, \tag{1}$$

where p is the pressure at the evaluation point, p_∞ is the pressure in the freestream, ρ is the fluid density, and U_∞ is the freestream velocity. The C_f value is calculated as

$$C_f = \frac{\tau_{wall}}{\frac{1}{2}\rho U_\infty^2}, \tag{2}$$

where τ_{wall} is the wall shear stress at the corresponding evaluation point. The validation shows that the CFD model can accurately predict the value of C_p and reasonably predict the value of C_f.

As observed in Figure 10, the hybrid RANS/LES model used in this paper produces C_p values that match closely with the previous CFD and experimental results presented by Jones et al. [17] except for small discrepancies at the tail, i.e., $x = 1.3$ m. These discrepancies between the predicted C_p obtained in the present CFD simulation and the experimental measurements by Jones et al. [17] tend to increase in the locations where the pressure gradient switches from favorable to adverse, and vice versa. Flows with adverse pressure gradients are known to be challenging for turbulence models. However, as suggested by the present results (Figure 10), the differences are very small and well within the range acceptable for engineering applications.

The discrepancies in the C_f predictions from CFD simulations by Jones et al. [17] and the present CFD simulations can be explained by differences in the computational mesh design and different turbulence models used in the present study and those in Jones et al. [17]. In the present study, a fine near-wall mesh spacing is used, which is critical for accurate prediction of the skin friction. It is observed that the present predicted C_f values are in good agreement with the experimental measurements of Jones et al. [17]. The skin friction values in the fully turbulent boundary layer, as investigated in the present study, are very small and sensitive to boundary conditions. Free-stream turbulence is an important factor affecting the turbulence structure in the boundary layers. It has been reported that an increase in the free-stream turbulence increases skin friction and heat transfer [18]. The boundary conditions setting used in the present simulations were set to reflect the corresponding turbulence intensity value reported in Jones et al. [17]. However, note that precise measurement and adjustment of turbulence intensity in an experimental setting is very difficult and is characterized by large uncertainties. It is expected that

the difference between the experimental values and the present predicted values of C_f (Figure 11) can be largely attributed to the effect of the free-stream turbulence.

4. Results and Discussion

The dynamic pressure distribution plots are presented in Figure 12. As presented in Figure 12c, the stagnation point of high pressure is located at the front face of the SST hull. The flow accelerates after the stagnation point and this results in a favorable pressure gradient, i.e., a decrease of pressure in the direction of flow as shown at the bow section. On the contrary, an adverse pressure gradient, i.e., an increase of pressure in the direction of flow is observed at the stern section. As presented in Figure 12e, the pressure increases at regions close to the propeller due to the deceleration of the flow. This adverse pressure gradient results in a loss of momentum in the boundary layer flow and could lead to flow separation. This is confirmed via a detailed examination of the regions near the propeller that reveals flow separation is occurring at the propeller. This leads to the formation of a low-pressure region around the front tip of the propeller shroud.

The skin friction distribution plots are presented in Figure 13. The skin friction accounts for approximately 42% of the total drag force on the SST hull. The high skin friction regions are located at the bow section and the stern section. These regions can be identified in Figure 13a,b. This high skin friction is caused by the local flow accelerations at these regions. Figure 13c shows the increased skin friction region around the searchlight housing at the front face of the SST hull. However, the surface area associated with this increase skin friction at the searchlight housing is less than 1% of the surface area of the hemispheric bow and less than 0.05% of the wetted surface area of the SST. Therefore, the contribution is negligible to the total drag force experienced by the SST.

Figure 14 shows the streamlines around the SST hull colored by the flow velocity magnitude. The streamlines are largely attached to the hull surface and separate from the surface at the stern section. In the area around the propeller shroud (Figure 15) the streamlines swirl due to the propeller rotation. Furthermore, there are small vortices on the leading edge of the propeller shroud indicating flow separation.

The power consumption of the SST is calculated to be 927 kW and can be powered by a small 1 MW propulsion system. The low power consumption is due to the moderately low hydrodynamic resistance and highlights the high efficiency of the SST.
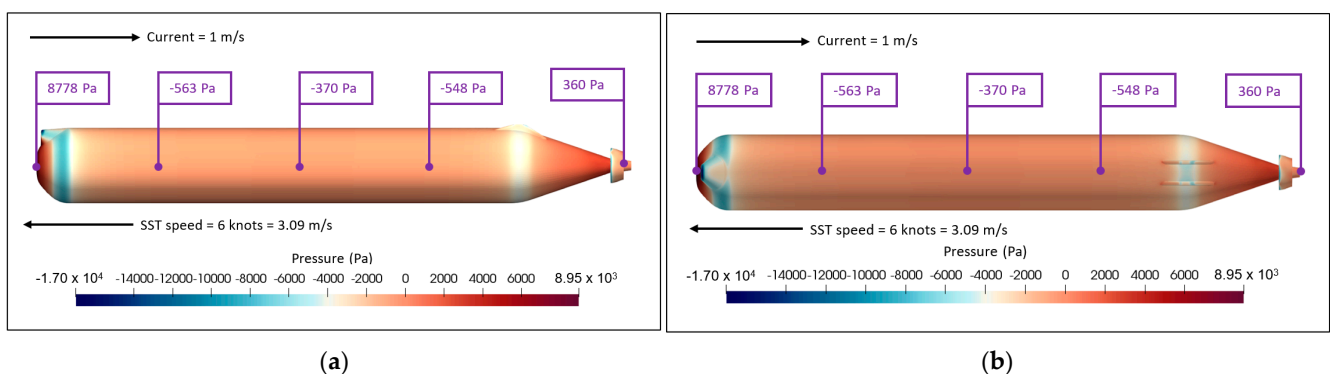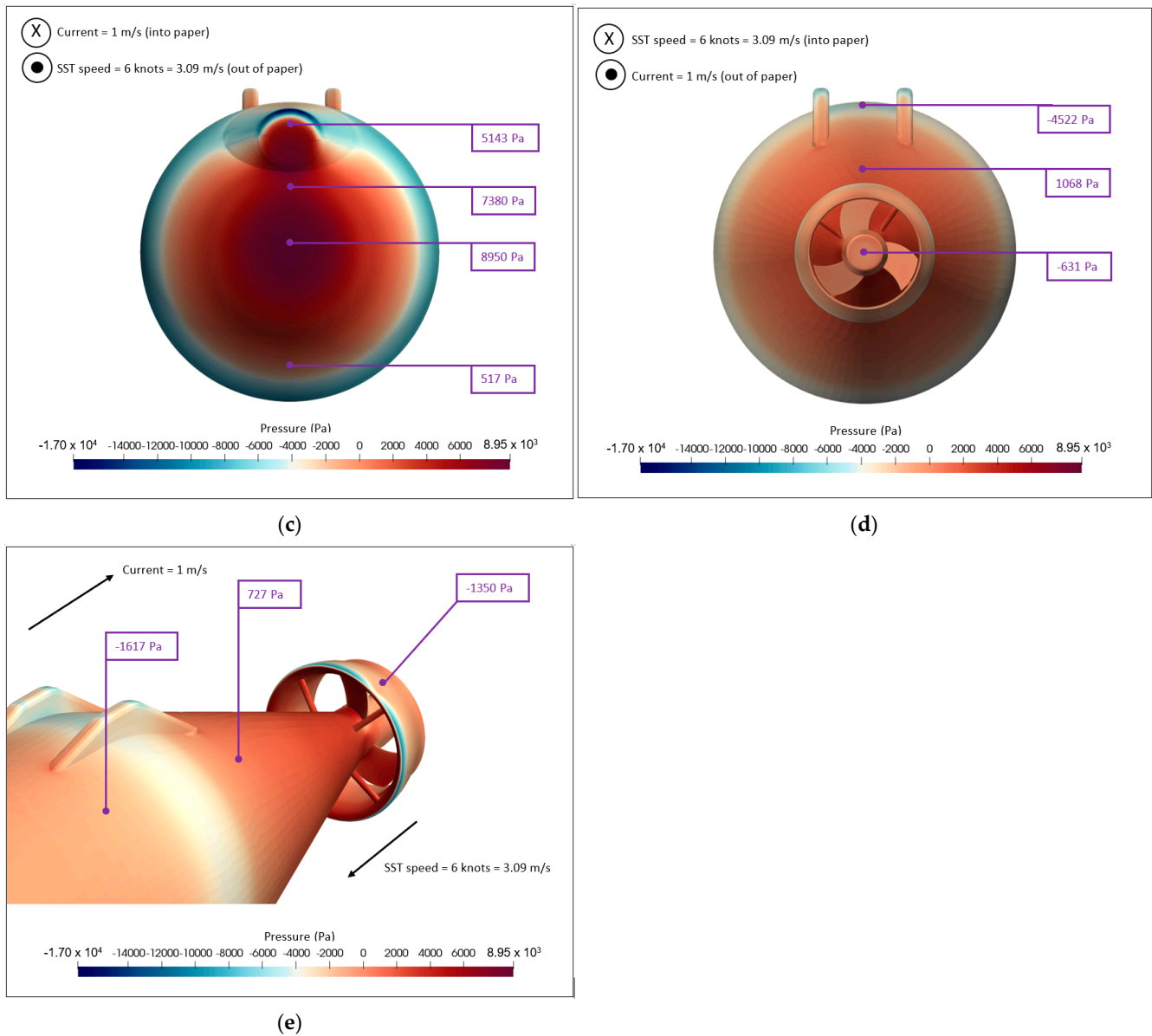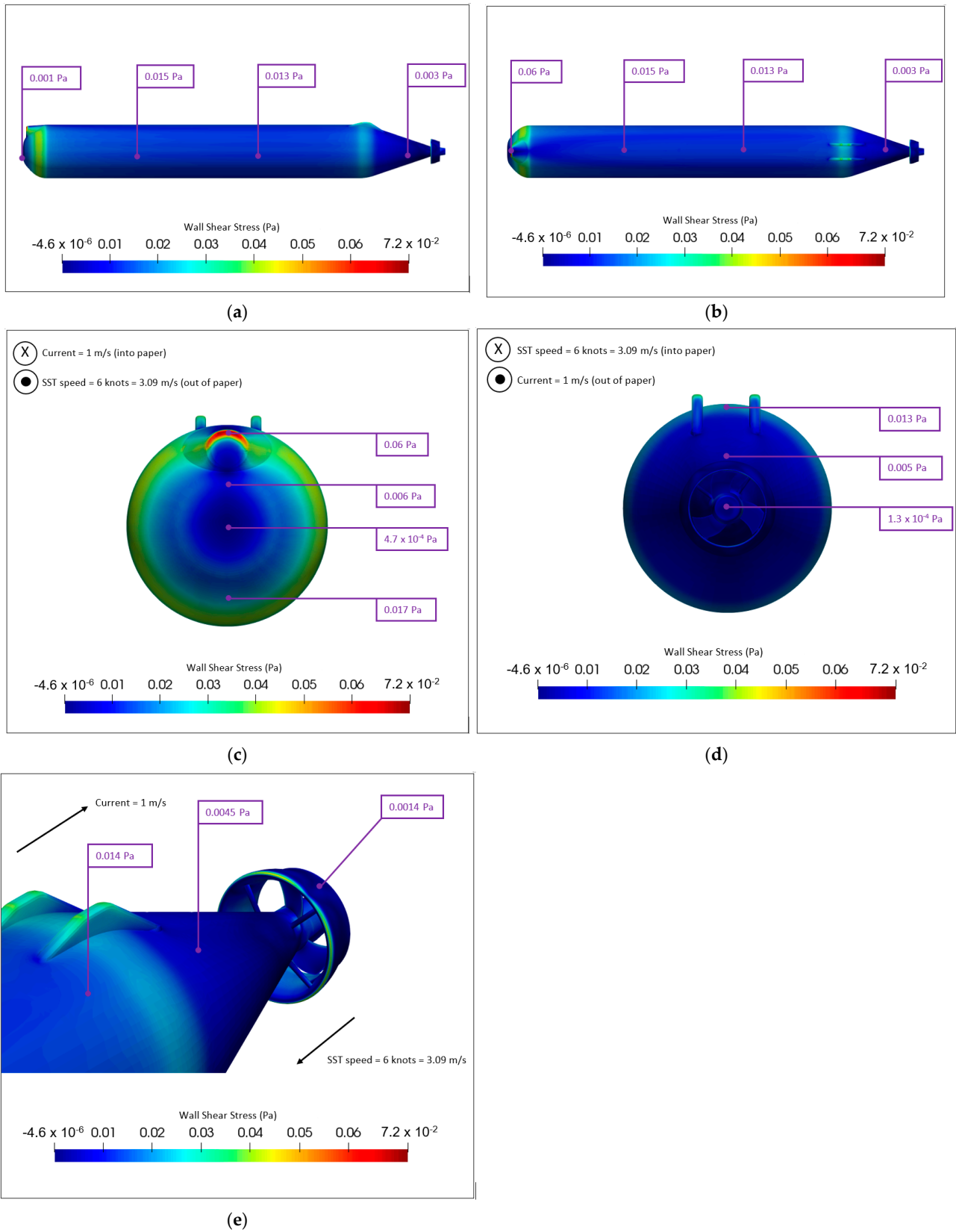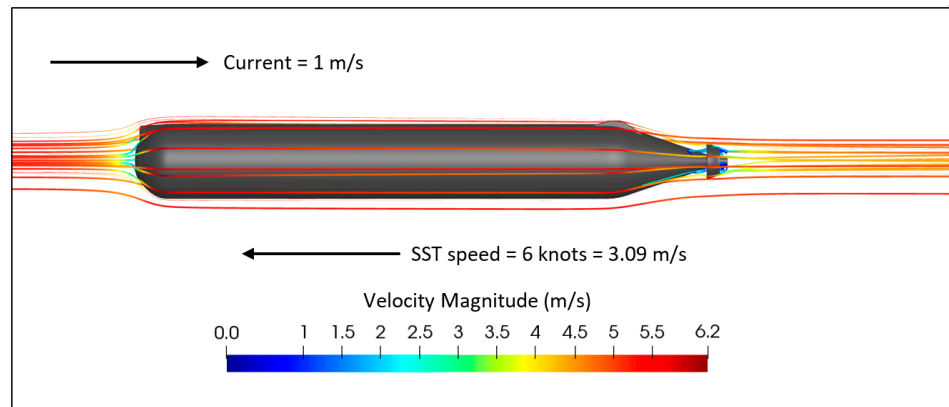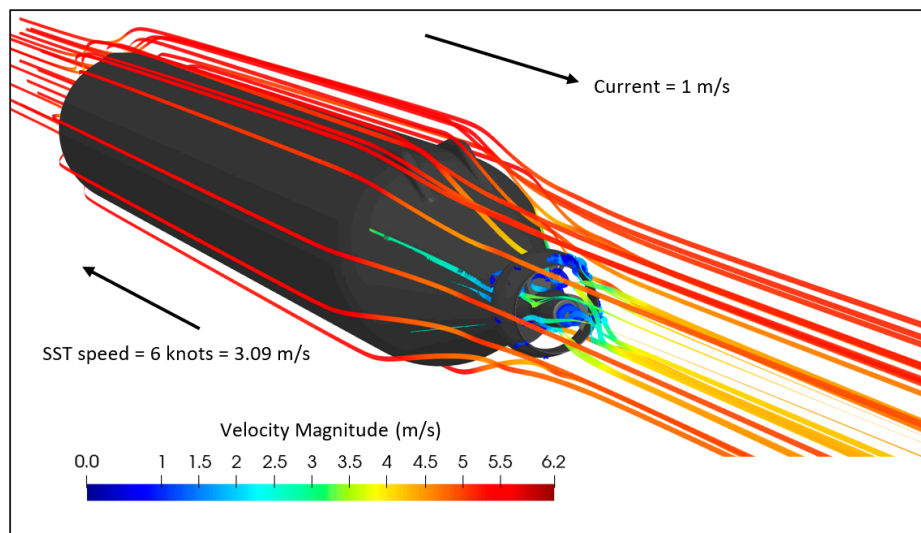

(a)

(b)

Figure 12. *Cont.*

(c)

(d)

(e)

Figure 12. Dynamic pressure distribution plots: (**a**) side view, (**b**) top view, (**c**) front view, (**d**) back view, and (**e**) zoom in at the propeller region.
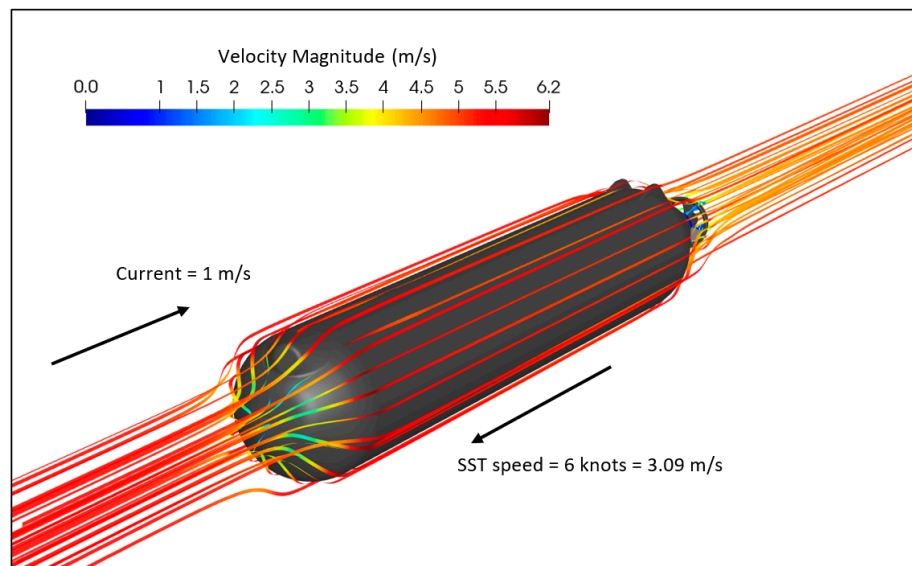
Figure 13. Skin friction distribution plots: (**a**) side view, (**b**) top view, (**c**) front view, (**d**) back view, and (**e**) zoom in at the propeller region.
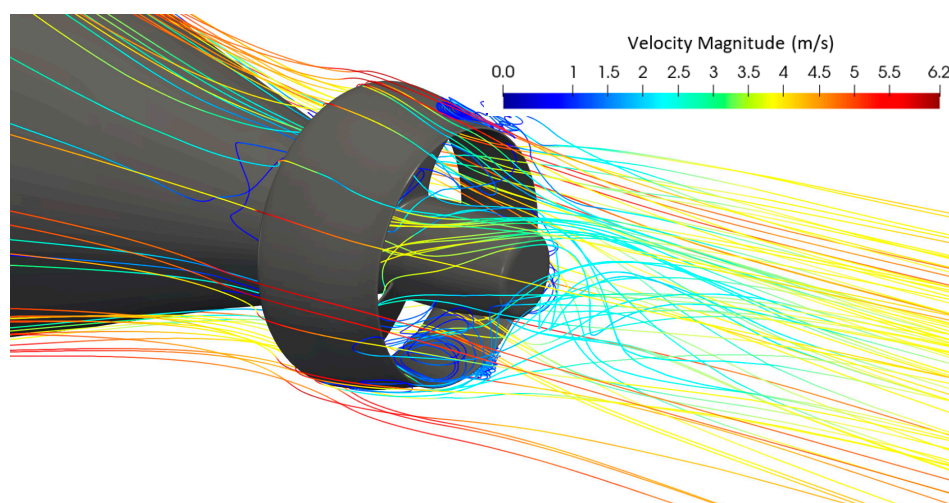
Figure 14. Streamlines around the SST hull colored by the flow velocity magnitude: (**a**) side view, (**b**) isometric view from the front, and (**c**) isometric view from the back.

Figure 15. Streamlines around the propeller shroud colored by the flow velocity magnitude.

5. Conclusions

The CFD simulations of the flow around the SST are presented. The study aims to provide accurate hydrodynamic forces of the SST moving with a specified operating forward speed of 6 knots (3.09 m/s) and subject to an incoming current velocity of 1 m/s. The force required to overcome forward resistance is calculated to be 222 kN when the subsea shuttle is travelling under this condition. The hydrodynamic forces predicted by the present model agree well with experimental measurements available in the open literature. The corresponding power consumption of the SST is calculated to be 927 kW which is low and means that the SST can be powered by a small 1 MW propulsion system. This highlights the high efficiency of the SST. The hybrid RANS/LES method presented in this paper is general and can be used for resistance optimization studies of any underwater vessel. Further, the method can also be utilized to study pressure distributions in shells which can be important in acoustic problems, e.g., Zarastvand et al. [19] and Asadijafari et al. [20].

Author Contributions: Conceptualization, Y.X., M.J.J., G.Y. and M.C.O.; Formal analysis, Y.X., M.J.J., G.Y. and M.C.O.; Investigation, Y.X., M.J.J., G.Y. and M.C.O.; Methodology, Y.X., M.J.J., G.Y. and M.C.O.; Resources, M.C.O.; Software, M.J.J. and G.Y.; Validation, Y.X., M.J.J., G.Y. and M.C.O.; Visualization, Y.X. and M.J.J.; Writing—original draft, Y.X. and M.J.J.; Writing—review & editing, Y.X., M.J.J., G.Y. and M.C.O. All authors have read and agreed to the published version of the manuscript.

Institutional Review Board Statement: Not applicable.

Informed Consent Statement: Not applicable.

Data Availability Statement: Not applicable.

Conflicts of Interest: The authors declare no conflict of interest.

References

1. Equinor. Subsea shuttle system. *Res. Discl.* **2019**, 662093.
2. Ellingsen, K.E.; Ravndal, O.; Reinås, L.; Hansen, J.H.; Marra, F.; Myrhe, E.; Dupuy, P.M.; Sveberg, K. Subsea shuttle system. *Res. Discl.* **2020**, 677083.
3. Xing, Y.; Ong, M.C.; Hemmingsen, T.; Ellingsen, K.E.; Reinås, L. Design Considerations of a Subsea Shuttle Tanker System for Liquid Carbon Dioxide Transportation. *J. Offshore Mech. Arct. Eng.* **2021**, *143*, 045001-1. [CrossRef]

4. Ma, Y.; Xing, Y.; Ong, M.C.; Hemmingsen, T.H. Baseline design of a subsea shuttle tanker system for liquid carbon dioxide transportation. *Ocean. Eng.* **2021**, *240*, 109891. [CrossRef]

5. Kretschmann, L.; Burmeister, H.-C.; Jahn, C. Analyzing the economic benefit of unmanned autonomous ships: An exploratory cost-comparison between an autonomous and a conventional bulk carrier. *Res. Transp. Bus. Manag.* **2017**, *25*, 76–86. [CrossRef]

6. CCSA. What Is CCS? Available online: http://www.ccsassociation.org/what-is-ccs/ (accessed on 30 December 2019).

7. IEA. *Energy Technology Perspectives 2010: Scenarios and Strategies to 2050*; OECD Publishing: Paris, France, 2010.

8. Weller, H.G.; Tabor, G.; Jasak, H.; Fureby, C. A tensorial approach to computational continuum mechanics using object-oriented techniques. *Comput. Phys.* **1998**, *12*, 620–631. [CrossRef]

9. Katsui, T.; Kajikawa, S.; Inoue, T. Numerical investigation of flow around a ROV with Crawleer based driving system. In Proceedings of the ASME 2012 31st International Conference on Ocean, Offshore and Arctic Engineering, Rio de Janeiro, Brazil, 1–6 July 2012.

10. Shang, Z.; Emerson, D.; Gu, X. Numerical investigations of cavitation around a high speed submarine using openfoam with les. *Int. J. Comput. Methods* **2012**, *9*, 1250040. [CrossRef]

11. Jones, D.A.; Chapuis, M.; Liefvendahl, M.; Norrison, D.; Widjaja, R. *RANS Simulations Using OpenFOAM Software*; DST-Group-TR-3204 Report; Maritime Platforms Division, DST Group Defence Science and Technology Group: Canberra, Australia, 2016.

12. Fureby, C.; Anderson, B.; Clarke, D.; Erm, L.; Henbest, S.; Giacobello, M.; Jones, D.; Nguyen, M.; Johansson, M.; Jones, M.; et al. Experimental and numerical study of a generic conventional submarine at 10° yaw. *Ocean Eng.* **2016**, *116*, 1–20. [CrossRef]

13. Xing, Y. A Conceptual Large Autonomous Subsea Freight-Glider for Liquid CO_2 Transportation. In Proceedings of the Volume 6: Ocean Engineering, ASME International, Virtual, Online, 21–30 June 2021.

14. Ellingsen, K.E.; Equinor, Stavanger, Norway. Personal Communication, 2019.

15. OpenFoam. The Open Source CFD Toolbox, User Guide v1812. 2018. Available online: https://www.openfoam.com/documentation/user-guide (accessed on 25 March 2020).

16. ASME. *ASME V V 20: Standard for Verification and Validation in Computational Fluid Dynamics and Heat Transfer*; ASME: New York, NY, USA, 2009.

17. Jones, M.B.; Erm, L.P.; Valiyff, A.; Henbest, S.M. *Skin Friction Measurements on a Model Submarine*; DSTO Report; Aerospace Division, Defence Science and Technology Organisation: Canberra, Australia, 2011.

18. Stefes, B.; Fernholz, H.-H. Skin friction and turbulence measurements in a boundary layer with zero-pressure-gradient under the influence of high intensity free-stream turbulence. *Eur. J. Mech.-B/Fluids* **2004**, *23*, 303–318. [CrossRef]

19. Zarastvand, M.R.; Ghassabi, M.; Talebitooti, R. Acoustic Insulation Characteristics of Shell Structures: A Review. *Arch. Comput. Methods Eng.* **2021**, *28*, 505–523. [CrossRef]

20. Asadijafari, M.; Zarastvand, M.; Talebitooti, R. The effect of considering Pasternak elastic foundation on acoustic insulation of the finite doubly curved composite structures. *Compos. Struct.* **2021**, *256*, 113064. [CrossRef]